Article

Not peer-reviewed version

Synthesis and Application of P(EDOT-co-Py)@MWCNT Hybrid as Cathode Electrode for Aqueous Aluminum-Ion Batteries

Glenda Ribeiro de Barros Silveira Lacerda , Luiz Paulo Fagundes dos Santos , Nathany Lopes de Oliveira Sousa , Gabriel Jácomo de Paula Tonon , Maria Luiza Miranda Rocco , Tulio Matencio , Hállen Daniel Rezende Calado , Paulo Fernando Riberiro Ortega , Garbas Anacleto dos Santos Junior *

Posted Date: 22 December 2025

doi: 10.20944/preprints202512.1852.v1

Keywords: nanohybrid; aluminium-ion storage device; conjugated polymer; carbon nanotube; P(EDOT-co-Py)

 doi:10.20944/preprints202512.1852.v1

Article

Synthesis and Application of P(EDOT-co-Py)@MWCNT Hybrid as Cathode Electrode for Aqueous Aluminum-Ion Batteries

Glenda R. de B. S. Lacerda [1], Luiz P. F. dos Santos [2], Nathany L. O. Sousa [2], Gabriel J. de P. Tonon [2], Maria L. M. Rocco [3], Tulio Matencio [1], Hállen D. R. Calado [1], Paulo F. R. Ortega [2] and Garbas A. dos Santos Junior [2,*]

[1] Departamento de Química/ICEx, Universidade Federal de Minas Gerais, Av. Antônio Carlos, 6627, Pampulha, CEP 31270-901, Belo Horizonte–MG, Brazil.

[2] Grupo de Estudos em Dispositivos de Armazenamento de Energia (GEDAE), Departamento de Química, Universidade Federal de Viçosa, Av. Peter Henry Rolfs, s/n Campus Universitário, CEP 36570-900, Viçosa–MG, Brazil

[3] Instituto de Química, Universidade Federal do Rio de Janeiro, Av. Athos da Silveira Ramos, 149, Cidade Universitária, CEP 21941-909, Rio de Janeiro–RJ, Brazil

* Correspondence: garbas.junior@ufv.br or garbas.anacleto@gmail.com

Abstract

A hybrid material based on the copolymerization of EDOT (3,4-ethylenedioxythiophene) and Py (pyrrole), 1:1 monomer ratio, onto multi-walled carbon nanotubes (MWCNTs) was synthesized through a multistep functionalization approach. The resulting P(EDOT-co-Py)@MWCNT hybrid, poly(3,4-ethylenedioxythiophene-co-pyrrol)@MWCNT hybrid, was characterized by Fourier-transform infrared spectroscopy (FTIR), Raman spectroscopy, X-ray photoelectron spectroscopy (XPS), and thermogravimetric analysis (TGA). These characterizations confirmed the successive functionalization steps, the effective anchoring of the monomers, and the subsequent formation of the copolymer. Transmission electron microscopy (TEM) images revealed a homogeneous polymer coating along the nanotube surface, while preserving the structural integrity of the MWCNTs throughout the functionalization and polymerization processes. The P(EDOT-co-Py)@MWCNT hybrid was evaluated as an active electrode material for aluminum-ion storage in aqueous aluminum sulfate electrolyte. The system exhibited two distinct charge-storage mechanisms: at high current densities, proton surface adsorption dominated, whereas at lower rates, a faradaic contribution associated with polymer chain redox activity and the reversible extraction/insertion of Al^{3+} became prevalent. The hybrid electrode delivered high specific capacities, reaching 200.6, 106.3, and 44.3 mAh g^{-1} at 0.10, 0.25, and 0.50 A g^{-1}, respectively. These values are comparable to—or even exceed—those reported for similar cathodic materials designed for Al^{3+} storage, highlighting P(EDOT-co-Py)@MWCNT hybrid as a highly promising cathode candidate for aqueous aluminum-ion energy-storage systems.

Keywords: nanohybrid; aluminium-ion storage device; conjugated polymer; carbon nanotube; P(EDOT-co-Py)

1. Introduction

There is a growing demand for energy storage systems that combine high-energy and power density with low cost and safety. Among these devices, lithium-ion batteries (LIBs) are the most widely commercialized, primarily due to their long cycle life and high-energy density. However, LIBs also face significant drawbacks, including safety concerns, high production costs, toxicity, and the limited availability of lithium resources [1], which are unevenly distributed worldwide [2] and often

 doi:10.20944/preprints202512.1852.v1

subject to geopolitical issues [3]. These limitations have motivated the search for alternative energy storage chemistries based on safer and more abundant elements [1].

In this context, beyond lithium, several other systems have been investigated, including sodium-, potassium-, magnesium-, calcium-, zinc-, and aluminum-ion batteries [4]. Within in this scenario, multivalent metal-ion-based systems offer notable advantages over monovalent cations, particularly due to their faster charge-transfer dynamics as well as higher energy density and capacity [5].

Among these alternatives, aluminum-based energy storage systems exhibit the highest theoretical capacity, attributed to the three-electron transfer during charge/discharge reactions. This results in an exceptionally high volumetric capacity (8046 mAh cm^{-3}), surpassing that of lithium (2062 mAh cm^{-3}). In terms of gravimetric capacity, however, aluminum (2980 mAh g^{-1}) falls below lithium (3870 mAh g^{-1}) [4]. Aluminum-ion batteries (AIBs) and aluminum-ion supercapacitors (AISCs) are also particularly attractive due to aluminum's abundance and the benefits of its well-established recycling infrastructure—an aspect that remains a major challenge for LIBs [3].

Despite these advantages, significant challenges remain. The strong electrostatic interaction between Al^{3+} and host materials often leads to irreversible insertion processes. Moreover, the combination of a small ionic radius and high charge density hinders desolvation [3,6]. Other issues reported for Al insertion materials include capacitive behavior, poor reversibility (low coulombic efficiency), short cycle life, and structural disintegration during ion insertion/extraction [7].

Various materials have been explored as active components in Al-ion storage systems, such as Prussian Blue Analogues (PBAs), including $KCu[Fe(CN)_6]\cdot 8H_2O$ [8]; chalcogenides ($Cu_{2-x}Se$) [9]; transition metal oxides such as VO_2 [10], Mg–MnO_2 [11], and TiO_2 [12]; NASICON-type $Na_3V_2(PO_4)_3$ [13]; and conducting polymers (CPs), such as poly(3,4-ethylenedioxythiophene):poly(4-styrenesulfonate) (PEDOT:PSS) [14], among others. Among Al-ion electrode materials, CPs have attracted particular attention due to their combination of electrical conductivity, environmental and thermal stability, light weight, processability, and low cost [15].

CPs have been extensively investigated in LIBs, providing a solid foundation for next-generation devices. Representative CPs include polyacetylene (PAc), polyaniline (PANI), poly(p-phenylene) (PPP), poly(p-phenylenevinylene) (PPV), polythiophene (PTh), poly(3,4-ethylenedioxythiophene) (PEDOT), and polypyrrole (PPy) [16–18]. The strong π–π donor–acceptor interactions in these materials enhance electronic properties, while their macromolecular structures, stabilized by non-covalent interactions, prevent dissolution and maintain structural integrity during redox reactions [15,19].

Although PANI is widely studied for its low cost and ease of synthesis, it can release carcinogenic benzidine upon degradation, leading to PEDOT one of the most environmentally friendly CPs [20]. PEDOT also exhibits high conductivity (up to 23.8 S cm^{-1} [18]), rapid polymerization reactions, excellent thermal and chemical stability, and a theoretical specific capacitance of 210 F g^{-1} [21]. The presence of sulfur atoms and the ethylenedioxy group enhances PEDOT's robustness, giving it an advantage over PANI and PPy [22]. However, it still has limitations, including strong S:O interactions and the relatively high monomer cost [22–25]. PEDOT has been studied as a possible cathode for AIBS, e.g., Ai et al. (2021) [14] fabricated PEDOT:PSS electrodes via evaporation–solidification on carbon cloth. Galvanostatic measurements using $Al_2(SO_4)_3$ electrolyte (1.2 mol L^{-1}) revealed faradaic reactions with Al^{3+}, yielding discharge capacities of 78, 59, 40, 25, 19, 12, and 9 mAh g^{-1} (269, 201, 138, 86, 64, 41, and 29 F g^{-1}) at current densities of 0.2–3 A g^{-1}, demonstrating its potential for AIBs.

Similarly, PPy is environmentally friendly [20], exhibiting fast kinetics, stability via charge delocalization, and reversible doping. Its charge storage relies on surface pseudocapacitance, with theoretical capacitance up to 620 F g^{-1} and conductivity ranging from 10^{-10} to 10^{-3} S cm^{-1}, which depends on the synthesis methodology [18]. Nonetheless, PPy suffers from rapid capacity fading caused by volumetric changes and the insertion/extraction of large anions, which may lead to structural collapse and poor cycling stability [26]. Additional challenges for PPy include discrepancies between theoretical and experimental performance [27].

 doi:10.20944/preprints202512.1852.v1

Strategies to overcome these limitations include improving conductivity [24] and mitigating volumetric changes in of the polymeric chains during charge and discharge processes [28], which includes copolymer formation, and hybridization with inorganic nanomaterials. Kadac et al. (2015) [24] first reported P(Py-co-EDOT), combining PEDOT's conductivity with pyrrole's low cost, showing higher conductivity (0.710 ± 0.003 μS m^{-1}) than PEDOT (0.488 ± 0.004 μS m^{-1}) and PPy (0.432 ± 0.004 μS m^{-1}). Sanmuigam et al. (2025) [29] developed a PEDOT–PPy copolymer for dopamine sensing, achieving lower charge-transfer resistance (68 Ω vs. PPy: 135 Ω, PEDOT: 112 Ω) and enhanced current response.

Composites and hybrid materials [30] can be fabricated by combining organic and inorganic components in precise ratios, including combinations of inorganic components, such as metal ions, graphene, carbon nanotubes, and oxides, with organic components like polymers and ligands. This process creates a synergistic effect where the final material leverages the properties of its constituents and gains new, enhanced properties [31,32]. Among nanocarbon materials, carbon nanotubes (CNTs) stand out due to their high aspect ratio, large surface area, and high electrical conductivity (single-walled carbon nanotubes (SWCNTs) ~10^4 S cm^{-1} and multi-walled carbon nanotubes (MWCNTs) 10^9–10^{20} S cm^{-1} [18]).

In CP/CNT composites, CNTs act as conductive additives, enhancing the electrochemical performance of energy storage systems [33]. This nanocarbon provides fast charge–discharge kinetics [34] and exhibits capacitive behavior, which, despite its low intrinsic capacitance, interacts electrostatically with the CP surface and via π–π stacking, improving electron transfer and overall capacitance. [28] CNTs also reinforce the composite mechanically, enhancing structural integrity and cycling stability [35].

Neat MWCNTs have been applied as cathode materials in AIBs. For example, Jiao et al. (2016) [36] employed MWCNTs with the ionic liquid $AlCl_3$–[EMIm]Cl (1-Ethyl-3-methylimidazolium chloride-aluminum chloride), achieving specific capacitances of 55 F g^{-1} at 0.15 A g^{-1} and 25.2 F g^{-1} at 0.50 A g^{-1}. Kong et al. (2025) [37] used a polypyrrole@CNT composite, synthesized via in-situ polymerization of PPy on CNTs and tested in the same electrolyte, which delivered discharge capacities of 137 mAh g^{-1} at 0.25 A g^{-1} and 100 mAh g^{-1} at 2 A g^{-1}.

Previously, we developed three CNT–CP hybrid nanomaterials for aqueous and organic Li-ion supercapacitors [31,38]. These hybrids were synthesized by chemically bonding the CP to the CNT surface, following surface functionalization to enable monomer attachment and polymerization. This approach facilitates interfacial electronic transport compared to conventional polymerizations based on π–π interactions alone. The hybrids—poly(3,4-ethylenedioxythiophene-co-3-(pyrrol-1-methyl)pyridine) (P(EDOT-co-PyMP)) [31], poly(3,4-ethylenedioxythiophene-co-methylpyrrole) (P(EDOT-co-MPy)), and P(EDOT-co-PyMP) [38]—demonstrated effective hybrid formation, particularly in retaining capacitance during cycling. Symmetric cells containing P(EDOT-co-PyMP) or P(EDOT-co-MPy) in 1 mol L^{-1} aqueous $LiClO_4$ retained ~70% of their capacity after 20,000 cycles, while the corresponding copolymers degraded completely after 10,000 cycles. The hybrid formation mitigates mechanical and electrochemical degradation caused by volumetric changes during cycling [38]. Testing P(EDOT-co-PyMP) hybrid in both aqueous and acetonitrile electrolytes (1 mol L^{-1} $LiClO_4$) showed capacitance retention of 90.4% and 91%, respectively, after 5,000 cycles.

In this study, we propose a hybrid designed P(EDOT-co-Py)@MWCNT, based on poly(3,4-ethylenedioxythiophene-co-pyrrole), synthesized by successive MWCNT functionalization followed by copolymerization of EDOT and Py in a 1:1 ratio. This strategy aims to combine the advantageous properties of PPy and PEDOT with the mechanical strength and conductivity of CNTs. The material was characterized by Fourier-transform infrared spectroscopy (FTIR), Raman spectroscopy, X-ray photoelectron spectroscopy (XPS), thermogravimetry analyses (TGA), and transmission electron microscopy (TEM). Its electrochemical performance as a positive electrode for aqueous aluminum-ion batteries was evaluated using cyclic voltammetry (CV), galvanostatic charge–discharge (GCD), and electrochemical impedance spectroscopy (EIS).

 doi:10.20944/preprints202512.1852.v1

2. Materials and Methods

2.1. Synthesis of P(EDOT-co-Py)@MWCNT Hybrid

The P(EDOT-co-Py)@MWCNT hybrid was prepared through a multistep procedure, as illustrated in **Scheme 1**. The procedure involved CNT oxidation (*i*), amidation (*ii*), monomer coupling (*iii*), and in situ copolymerization (*iv*). Each step was designed to functionalize the CNT surface and promote efficient polymer growth.

Initially, MWCNTs (CTNANO, Brazil, >95 wt.%) were oxidized using a concentrated H_2SO_4/HNO_3 mixture (3:1, v/v), then washed and dried to obtain oxidized MWCNTs (MWCNT−ox). Next, MWCNT-ox was functionalized with 1,3-diaminopropane (DAP) via microwave-assisted amidation. Briefly, 1.5 g of MWCNT−ox was dispersed in 100 mL of DAP and ultrasonicated for 10 min. The reaction was carried out at 100 °C and 100 W for 30 min under reflux. The resulting MWCNT−ox−DAP was filtered, washed with ethanol, and dried at 100 °C for 3 h.

Before in situ polymerization, monomer coupling was performed through thionyl chloride activation of carboxylic acids. MWCNT−ox−DAP (0.50 g) was dispersed in 18 mL of anhydrous dichloromethane, sonicated for 30 min, cooled to ~0 °C, and treated with 2 mL of triethylamine. A solution of 3-thiophene carbonyl chloride (TCC, prepared as described elsewhere [39]) in 4 mL of dichloromethane, was added dropwise over 30 min, followed by stirring for 3 h. The product, MWCNT−ox−DAP−ATC, was collected by filtration, washed with anhydrous dichloromethane, and dried at 100 °C for 3 h.

Finally, the P(EDOT-co-Py)@MWCNT hybrid was synthesized by dispersing MWCNT−ox−DAP−ATC (0.015 g mL^{-1}) in anhydrous chloroform and sonicated for 30 min in a three-necked flask equipped with a reflux condenser and addition funnel. An equimolar mixture of EDOT and pyrrole (1:1, 0.06 mol L^{-1}) was added dropwise, followed by $FeCl_3$ (0.038 g mL^{-1} in chloroform). The polymerization was carried out at room temperature under nitrogen with continuous stirring for 24 h. The hybrid was collected by filtration through a PTFE (Polytetrafluoroethylene) membrane, washed with methanol, and further purified by Soxhlet extraction with methanol for 48 h.

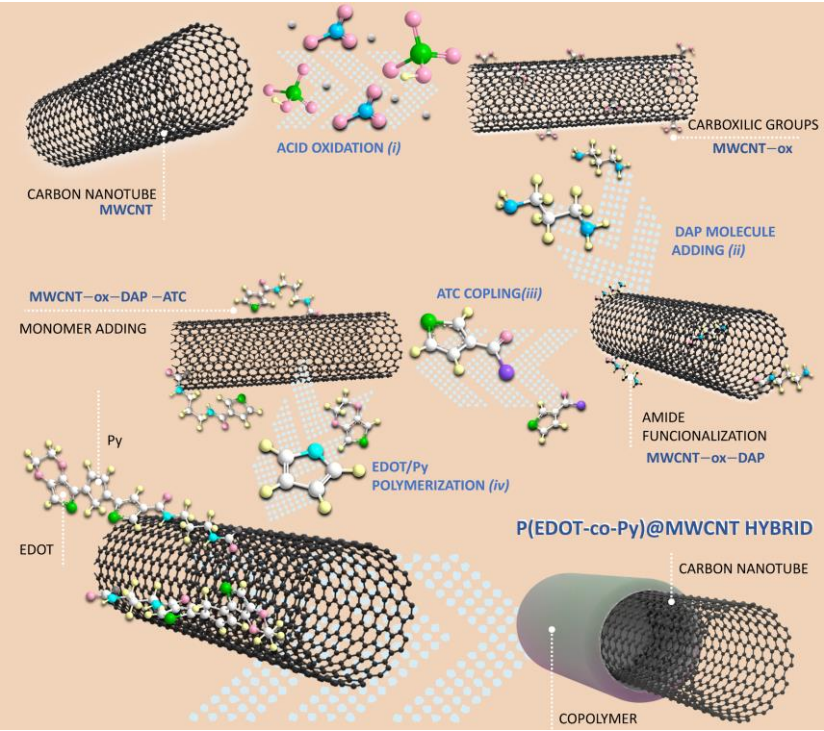

Scheme 1. – P(EDOT-co-Py)@MWCNT hybrid synthesis steps.

 doi:10.20944/preprints202512.1852.v1

2.2. Material Characterization

The obtained P(EDOT-co-Py)@MWCNT hybrid and its precursor materials were characterized using different techniques. Fourier Transform Infrared (FTIR) spectra were recorded with a Thermo Scientific Nicolet 380 spectrometer. The samples were prepared as KBr pellets, and spectra were collected in transmission mode with 128 scans. Raman spectra were acquired using a Witec Alpha 300 R Confocal Raman Microscope. A 633 nm laser (~2.3 mW) was used for the functionalized CNTs, while a 532 nm laser (~2 mW) was employed for the hybrids and copolymer. A VG Scientific Escalab 220-ixL system was employed to conduct X-ray photoelectron spectroscopy (XPS) measurements at room temperature, using a monochromatic Al Kα X-ray source (1486.6 eV) and a vacuum chamber base pressure of 2×10^{-9} mbar. While high-resolution spectra in the C1s, N1s, O1s, and S2p regions were gathered with 0.1 eV steps, survey spectra were obtained with a step size of 1 eV over the 0–1000 eV range. The electron energy analyzer was operative in large-area mode, with pass energies of 50 eV for survey scans and 20 eV for high-resolution scans. All the spectra were fit together using both Gaussian and Lorentzian functions. A Q5000 thermogravimetric analysis device (TA Instruments) was used to assess the thermal stability of functionalized carbon nanotubes, hybrids, and copolymers. Each sample was heated from room temperature to 800 °C at 10 °C min^{-1}, with a 25 mL synthetic air flow. Transmission electron microscopy (TEM) images were obtained using a Tecnai G2-12 Spirit Biotwin FEI, at 120 kV. Electrical conductivity tests were conducted using a four-probe method (Universal Probe Jandel - Engineering Ltd.). Leighton Buzzard—couplet to Keithley 238). Before the measurements, P(EDOT-co-Py) and P(EDOT-co-Py)@MWCNT hybrid were dried in an oven for 24 h (70 °C) and then pressed into 1 mm thick pellets.

2.3. Preparation of the Electrodes

The working electrodes were prepared using the hybrid polymer as the active material, carbon black (C-nergy Super C65 - Nanografi), and polyvinylidene fluoride (PVDF, Sigma-Aldrich) as the binder. The components were mixed in an agate mortar at a mass ratio of 80:10:10. N-methyl-2-pyrrolidone (NMP, Sigma-Aldrich, 98%) was then added as the solvent to form a homogeneous slurry, which was stirred overnight using a magnetic stirrer. The resulting slurry was applied onto graphite rods and dried overnight at 70 °C.

2.4. Electrochemical Characterization

The electrochemical performance of the P(EDOT-co-Py)@MWCNT hybrid was evaluated using a three-electrode configuration assembled in T-type Swagelok cells. All measurements were conducted on a VMP3 potentiostat (BioLogic).

GCD measurements were performed at current densities ranging from 0.1 to 2 A g^{-1}. CV was conducted at scan rates between 0.50 and 50 mV s^{-1} within a potential window of −0.2 to 0.6 V versus Ag/AgCl (3.5 mol L^{-1} KCl). GCD were conducted under the same potential range, at 0.10, 0.25, 0.50, 0.80, 0.90, 1.00, and 2.00 A g^{-1}. Electrochemical impedance spectroscopy (EIS) was carried out using a ±5 mV amplitude signal over a frequency range of 500 kHz to 50 mHz.

For all tests, the cells employed a graphite rod as the counter electrode, an Ag/AgCl (3.5 mol L^{-1} KCl) reference electrode, and glass fiber as the separator. The electrolyte consisted of a 1.2 mol L^{-1} aqueous $Al_2(SO_4)_3$ solution acidified with H_2SO_4, pH of 1.5.

Specific capacitance (C_{sp}), energy density (E_{sp}), power density (P_{sp}) and coulombic efficiency (ε) were calculated from the galvanostatic data using equations 1-4.

$$C_{sp} = \frac{2I(\int V dt)_{discharge}}{(m)V^2_{discharge}} \quad (1)$$

$$E_{sp} = \frac{I \int V\, dt}{m} \quad (2)$$

 doi:10.20944/preprints202512.1852.v1

$$P_{sp} = \frac{E_{sp}}{\Delta t_{discharge}} \quad (3)$$

$$\varepsilon = \frac{\Delta t_{discharge}}{\Delta t_{Charge}}\ x\ 100 \quad (4)$$

where *I* refers to the applied current, t is the time, V refers to the potential, and m refers the active mass of the electrode and $V_{discharge}$ is the maximum potential at the end of the discharge, after the ohmic drop.

3. Results and Discussion

3.1. Material Characterization

The P(EDOT-co-Py)@MWCNT hybrid was obtained through sequential synthesis steps. **Figure 1(A)** presents the FTIR spectra of MWCNT — ox, MWCNT — ox — DAP and MWCNT — ox — DAP — ATC, while Figure 1(B) presents the FTIR spectra for P(EDOT-co-Py) copolymer and P(EDOT-co-Py)@MWCNT hybrid, along with the spectrum of MWCNT—ox—DAP—ATC for comparison. All synthesis step is summarized in **Scheme S1**.

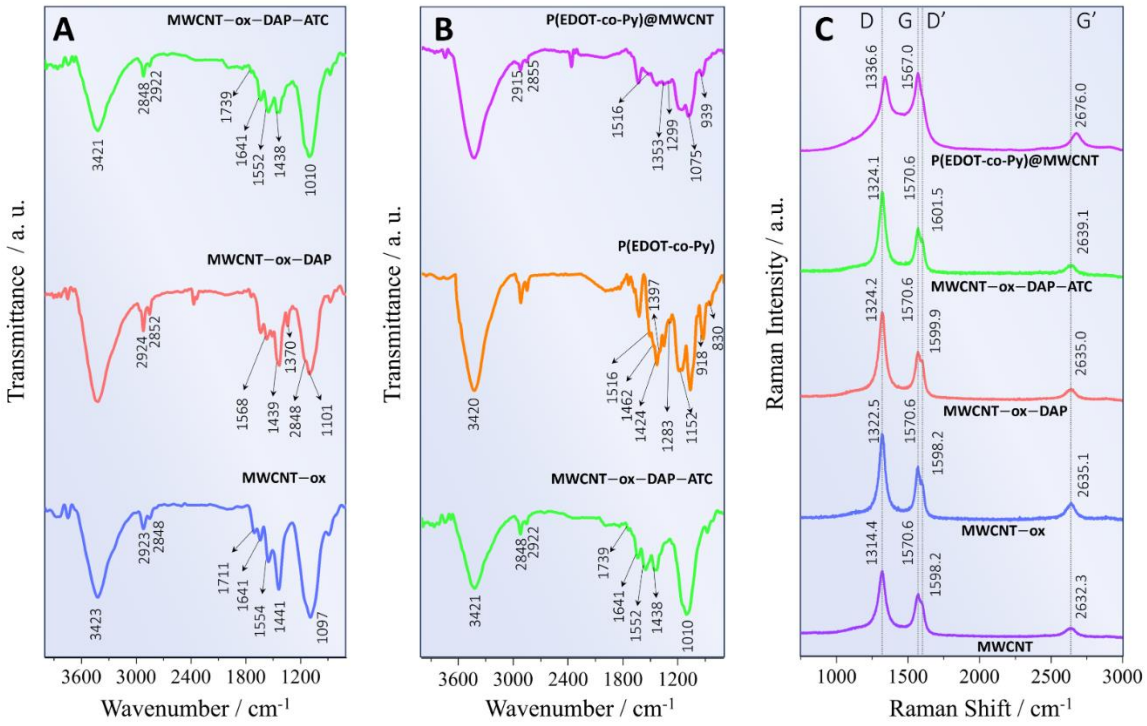

Figure 1. – FTIR spectra for (A) MWCNT, MWCNT — ox — DAP and MWCNT — ox — DAP — ATC; (B) MWCNT — ox — DAP — ATC, P(EDOT-co-Py) and P(EDOT-co-Py)@MWCNT hybrid. (C) Raman spectra for MWCNT, MWCNT—ox, MWCNT—ox—DAP, MWCNT—ox—DAP—ATC, P(EDOT-co-Py) and P(EDOT-co-Py)@MWCNT hybrid.

The MWCNT—ox spectrum, **Figure 1(A)**, exhibits characteristic absorption bands at 3423, 2923, 2848, 1711, 1641, 1554, 1441, and 1097 cm^{-1}. The bands at 2923 and 2848 cm^{-1} correspond to C–H (sp^3) stretching vibrations, while the signal at 1441 cm^{-1} is assigned to C=C stretching [40]. The remaining features are associated with functional groups introduced during the oxidation process, mainly O–H and C=O. The broad band centered at 3423 cm^{-1} is attributed to O–H stretching, originating from adsorbed water molecules and hydroxyl or carboxylic groups (–COH and –COOH) [41]. The

 doi:10.20944/preprints202512.1852.v1

absorptions at 1097 and 1711 cm^{-1} are ascribed to C–O and C=O stretching vibrations, respectively [42].

In the second synthesis step, an amine coupling reaction occurs, in which DAP reacts with the carboxylic groups present on the oxidized CNT surface, leading to amide functionalization of the nanotubes. The FTIR spectrum of MWCNT − ox − DAP retains the characteristic bands of MWCNT−ox, including the signal at 1439 cm^{-1} (C=C stretching) and the C–H stretching bands at 2924 and 2852 cm^{-1}. The increase in intensity of these C–H bands indicate the incorporation of DAP molecules, which introduce additional aliphatic C–H bonds onto the MWCNT−ox surface. The band at 1101 cm^{-1}, associated with C–O stretching vibrations, also remains visible [42]. A new band appearing at 1568 cm^{-1} is attributed to the secondary amine (N–H) group introduced onto the CNT surface [43]. In addition, the peak at 1370 cm^{-1} confirms the formation of amide bonds between the carboxylic groups of the oxidized CNTs and the amino groups of DAP [44]. For the last CNT functionalization step, a low-intensity band at 820 cm^{-1} is observed, corresponding to the C–S stretching vibration, confirming the ATC monomer coupling, **Figure S1** [45–47].

Figure 1(B) shows the FTIR spectra of the P(EDOT-co-Py)@MWCNT hybrid. For better comparison, the spectrum of the P(EDOT-co-Py) copolymer is also included, while the spectra of the individual PEDOT and PPy polymers are provided in the Supplementary Material, **Figure S2(A)** and **(B)**, respectively.

The PEDOT spectrum, **Figure S2(A)**, displays the characteristic absorption bands of its polymer backbone. The asymmetric C=C stretching of the benzoid heterocyclic structure appears at 1520 cm^{-1} [48], while the C–H stretching mode is observed at 1479 cm^{-1} [29]. The C–O–C stretching vibrations of the EDOT ring are detected at 1190 and 1075 cm^{-1} [48]. Additionally, the thiophenic ring stretching vibration occurs at 2379 cm^{-1} [49] and the (C–S) ring deformation band at 927 cm^{-1}. The signal at 1641 cm^{-1} is associated with C=N and –OH stretching, as well as N–H deformation modes [50].

The PPy spectrum, **Figure S2(B)**, also exhibits the typical absorption bands of polypyrrole. The C=C and C–H related vibrations appear at 1048, 780, and 686 cm^{-1} [51], the latter also corresponding to C–C out-of-plane aromatic ring bending of the PPy skeleton [52]. The C=N stretching band is observed at 1477 cm^{-1} [51], and the characteristic stretching of the five-membered pyrrole ring appears at 1561 cm^{-1} [52]. Furthermore, a broad band centered at 3399 cm^{-1} corresponds to the N–H stretching mode [53].

Similar to the pristine PPy and PEDOT spectrum, the FTIR spectrum of the P(EDOT-co-Py)@MWCNT hybrid confirms the chemical functionalization and the formation of the hybrid through the coexistence of characteristic peaks from both polymers, frequently accompanied by small frequency shifts that indicate strong interactions, such as π - π^* [54]. In the case of the copolymer, in addition to these peaks, there are some new ones corresponding to the interaction of the monomers [55]. The presence of PEDOT, specifically its thiophene ring component, is evidenced by the conjugated C=C and C–C stretching bands at 1516 cm^{-1} and 1462 cm^{-1} [56]. The broad peak at 1070 cm^{-1} indicates a C–O–C tensile vibration [48], and bands at 918, 830, and 683 cm^{-1} are ascribed to the C–S bond in the thiophene ring [57]. Concomitantly, the integration of PPy into the hybrid structure is confirmed by characteristic pyrrole ring vibrational peaks. Specifically, the strong band at 1424 cm^{-1} corresponds to the N–C asymmetric stretching vibrational modes of the PPy ring. Furthermore, the peak observed at 1283 cm^{-1} is consistent with C–H and N–H stretching vibrations within the PPy structure [58]. The presence of the C=C benzenoid heterocycle vibration at 1462 cm^{-1} can be attributed to the existence of the n-doped state of the homopolymers [59]. Finally, the intense band centered at 3420 cm^{-1} is characteristic of the pyrrole's N–H stretching mode, which overlaps with the O–H stretching vibration from adsorbed moisture or hydroxyl groups [60].

For the P(EDOT-co-Py)@MWCNT hybrid, the FTIR spectrum confirms the incorporation of both polymeric and CNT components, including the bands at 2915 and 2855 cm^{-1} attributed to C–H stretching vibrations. The successful formation of the P(EDOT-co-Py) copolymer is evidenced by characteristic peaks from both PEDOT and PPy units. The PEDOT component is confirmed by the conjugated C=C and C–C stretching bands of the thiophene ring at 1516 cm^{-1} and 1353 cm^{-1},

 doi:10.20944/preprints202512.1852.v1

respectively. Furthermore, the C–C tensile vibration of the EDOT unit contributes to the band at 1075 cm^{-1}, which also corresponds to C–O stretching from the CNT. The presence of the peak at 1299 cm^{-1} is indicated as C–H and N–H stretching vibrations within the PPy [61]. Additionally, the C–S bond in the thiophene ring is ascribed to the band at 939 cm^{-1}. The coexistence of these distinct spectral features confirms the chemical functionalization and the formation of the P(EDOT-co-Py)@MWCNT hybrid [57].

Figure 1(C) presents the Raman spectra of the P(EDOT-co-Py)@MWCNT hybrid, along with those of the P(EDOT-co-Py) copolymer, MWCNT − ox, MWCNT − ox − DAP and MWCNT−ox−DAP−ATC. In the first stage of the synthesis, the MWCNT−ox sample exhibits three main peaks at 1322.5, 1570.6, and 2635.1 cm^{-1}, corresponding to the D, G, and G′ bands, respectively. A slight shoulder at 1598.2 cm^{-1} can also be observed near the G band, which is assigned to the D′ band. All these bands are characteristic of the CNT structure and are also observed in pristine MWCNTs before the acid oxidation process [62]. For pristine CNTs, the corresponding bands appear at 1314.4 (D), 1570.6 (G), 1598.2 (D′), and 2632.3 cm^{-1} (G′).

The D band, often referred to as the disorder band, is associated with the A_{1g} symmetric stretching mode and arises from defects and structural disorder within the carbon nanotubes [62]. The G band, known as the graphitic band, corresponds to the tangential vibration of the E_{2g} phonon mode of the sp^2 carbon network. [63] Meanwhile, the G′ band (also called the 2D band) results from a second-order scattering process of the D band and is related to the stacking order of graphene layers within the CNTs [62]. The D′ band, in turn, is associated with the effects of lattice distortion and finite-size disorder [64].

The I_D/I_G ratio provides information about the degree of structural order in the graphitic framework of the CNTs [62]. A higher I_D/I_G value indicates an increased amount of amorphous carbon, reflecting greater structural disorder. [65] These values for all materials are shown in **Table S1**. It can be observed that oxidation of the carbon nanotubes (MWCNT−ox, I_D/I_G = 1.07) leads to a slight decrease in structural order compared to pristine MWCNT (I_D/I_G = 1.03). This behavior is related to the oxidation process, which introduces oxygen-containing groups such as hydroxyl and carboxyl on the CNT surface, generating surface defects. The small variation observed in the I_D/I_G ratio suggests that the main CNT structure remains largely preserved after oxidation [64]. Subsequent CNT functionalization by DAP and ATC attachment leads to a slight increase in the I_D/I_G ratio to 1.10, indicating minor additional structural disorder.

P(EDOT-co-Py) Raman spectra is presented in **Figure S3**. The band at 1339.6 cm^{-1} is associated with the ring stretching vibrations of the C−C bonds for the PPy structure (D band) and the band at 1557.3 cm^{-1} is related to the π conjugated structure and C=C backbone stretching mode (G band). The observed band is a characteristic band for the C_α=C_β tensile vibration in the thiophene ring of the PEDOT chain [66].

The Raman spectrum of the hybrid material, **Figure 1(C)**, displays three main bands characteristic of CNTs, located at 1336.6 cm^{-1} (D), 1567 cm^{-1} (G), and 2676.0 cm^{-1} (G′). A noticeable shift is observed for the D band compared to the MWCNT−ox−DAP−ATC sample (1324.2 cm^{-1}), indicating that encapsulation of CNTs by the P(EDOT-co-Py) copolymer results in strong interactions between the polymer matrix and the CNT surface. These interactions modify the local electronic environment of the CNTs, requiring higher energy for the corresponding vibrational modes [67].

XPS for the P(EDOT-co-Py)@MWCNT hybrid and its precursors, along with P(EDOT-co-Py), are presented in **Figure 2(A)**. The main elements of interest were analyzed, and their specific spectra—C 1s, O 1s, N 1s, S 2s, and S 2p—are presented in **Figure 2(B-E)** for P(EDOT-co-Py)@MWCNT hybrid. The spectra for MWCNT−ox, MWCNT−ox−DAP, MWCNT−ox−DAP−ATC and P(EDOT-co-Py) can be seen in **Figure S4(A-H)**. Every sample exhibits the C1s photoemission peak, which is associated with the C–C bond and is centered at about 285 eV. The oxidation step of the CNTs and, in the case of the copolymers, the C–O–C linkage from the EDOT units is linked to the O1s peaks, which appear at 532 eV. Consequently, the P(EDOT-co-Py), P(EDOT-co-Py)@MWCNT hybrid, MWCNT − ox − DAP and MWCNT − ox − DAP − ATC exhibit the anticipated N1s peak at

 doi:10.20944/preprints202512.1852.v1

approximately 398 eV. This signal is related to the presence of pyrrole units for P(EDOT-co-Py) and amine functionalization for MWCNT−ox−DAP and MWCNT−ox−DAP−ATC and both for the P(EDOT-co-Py)@MWCNT hybrid material.

The presence of EDOT caused the S 2s (228 eV) and S 2p (164 eV) peaks to be found in the copolymer and hybrid sample. The thiophene ring from the ATC monomer unit, is present for the MWCNT−ox−DAP−ATC sample. The atomic percentages of the elements derived from the wide-scan XPS spectra are summarized in **Table S2**. These results evidence the successful functionalization in the MWCNT at each synthesis step and are consistent with the complementary results obtained from FTIR and Raman spectra.

Table S3 displays the binding energy assignments for the C 1s photoemission peaks, which were determined through the deconvolution of the XPS spectra shown in **Figure S4(A-H)**. The XPS spectra for the C 1s, O 1s, N 1s, and S 2p regions of - XPS spectra for MWCNT−ox−DAP − ATC and P(EDOT-co-Py)@MWCNT.

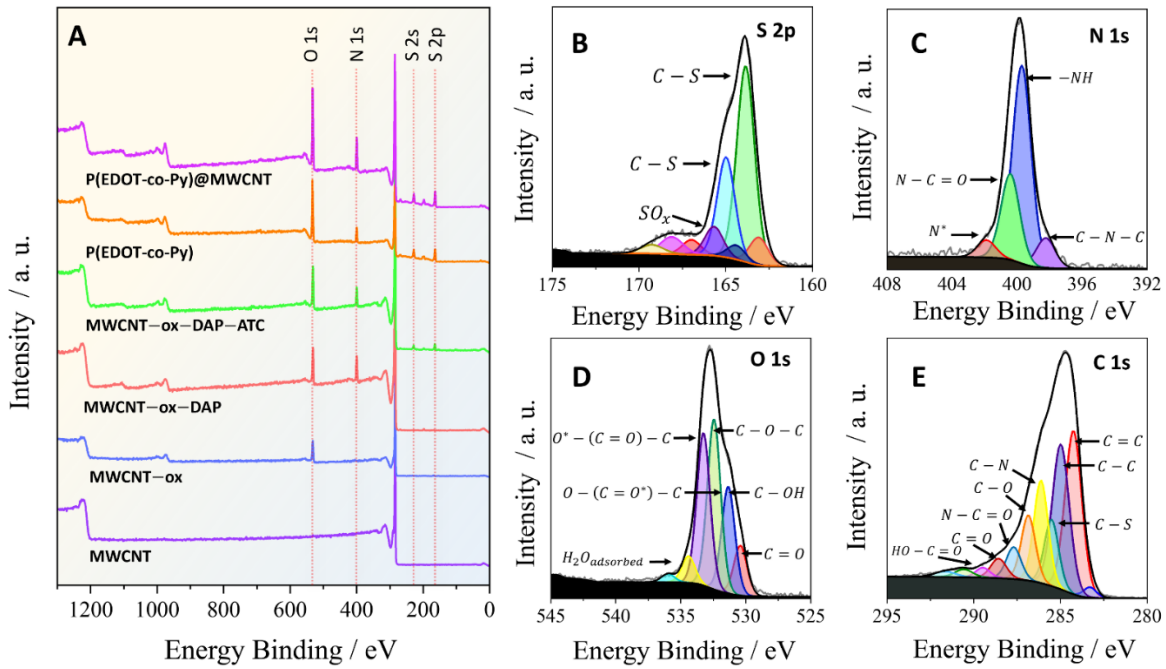

Figure 2. A) XPS spectra for MWCNT, MWCNT−ox, MWCNT−ox−DAP and MWCNT−ox−DAP−ATC, P(EDOT-co-Py) and P(EDOT-co-Py)@MWCNT hybrid; (B) XPS spectra of S 2p, N 1s, O 1s and C 1s, O 1s and N 1s of P(EDOT-co-Py)@MWCNT hybrid.

Approximately 285 eV is the center of the main C 1s peak for all samples. Because of variations in the atoms' electronegativity, peaks for C=C, C–C, and C–S bonds appear at lower binding energies than those for C–N and C–O.

The findings suggest that covalent bonds have been established between the functionalized CNTs and the copolymers. When comparing the hybrid samples to MWCNT−ox−DAP−ATC, the C 1s photoemission peak at 285.5 eV, which is primarily attributed to C–S contributions, broadens and intensifies, confirming the covalent attachment between the copolymer and CNT [68]. Furthermore, π–π* electronic transitions are responsible for a satellite peak at roughly 290.9 eV observed in all samples [69].

Table S4 lists the atomic percentages of the various carbon bonding states and the spectral deconvolutions of O 1s. The peak at approximately 534 eV is attributed to surface-adsorbed oxygen-containing groups or residual acidic species from the oxidation reactions and is associated with O–H bonds. Additional contributions were identified, including C=O at approximately 530 eV (carbonyl groups), C–O–C at approximately 532 eV (ether linkages), and C=O at approximately 533 eV

 doi:10.20944/preprints202512.1852.v1

(carbonyl groups in esters, amides, or anhydrides). Additionally, peaks in the N 1s spectra are seen at about 398 eV and 400 eV, which represent amine and amide species, respectively. The amine and the carboxylic groups of the thiophene monomer unit have established covalent bonds, as evidenced by these results [70]. The amine and amide peaks in MWCNT—ox—DAP exhibit comparable intensities. In contrast, the amide peak area in MWCNT—ox—DAP—ATC is significantly larger, thereby verifying the successful amidation step.

The presence of thiophene in the hybrid samples is further confirmed by the photoemission peaks in the S 2s (~228 eV) and S 2p (~164 eV) regions, which show the covalent bond between the copolymers and the CNTs [68].

Figure 3 displays the TGA and thermogravimetric derivative (dTG) curves for MWCNT, MWCNT-ox, MWCNT-ox-DAP, MWCNT-ox-DAP-ATC, P(EDOT-co-Py), and P(EDOT-co-Py)@MWCNT hybrid.

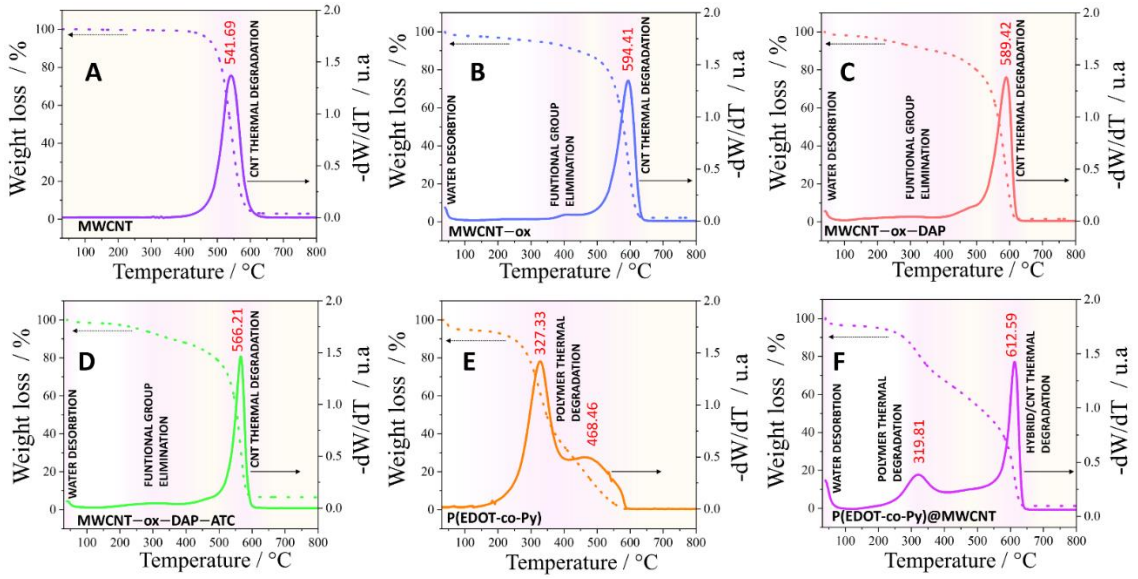

Figure 3. – TGA and dTG curves for (A) MWCNT, (B) MWCNT — ox, (C) MWCNT — ox — DAP, (D) MWCNT—ox—DAP—ATC, (E) P(EDOT-co-Py), and (F) P(EDOT-co-Py)@MWCNT hybrid.

The pristine MWCNT, **Figure 3(A)**, shows a single thermal event corresponding to its thermal breakdown. The degradation rate reaches its maximum at 541.7 °C, leaving a 4.5% residual mass [71]. After oxidation, **Figure 3(B)**, the MWCNT—ox sample undergoes a three-step decomposition process. Adsorbed water is lost during the initial stage, which takes place between 100 and 120 °C (approximately 2% loss). Decomposition of oxygen-containing functional groups produced during the oxidation and functionalization of CNTs is responsible for the second stage, which occurs in the 120–400 °C range (≈5.3% loss). The thermal decomposition of the CNT framework is characterized by the final stage with a maximum degradation rate at 594.4 °C [72].

Three degradation events are also noted for MWCNT—ox—DAP, **Figure 3(C)**. First, a 4% loss is due to the desorption of adsorbed water. Between 120 °C and 400 °C, the second stage exhibits a 9.0% mass loss rate, with the highest degradation rate at 302 °C, due to the elimination of nitrogen- and oxygen-containing functional groups [72]. This conduct validates the successful amidation and improved surface functionalization. The last step in breaking down, which happens at 589.4 °C, is linked to CNT combustion [73]. In the 120–400 °C range, the MWCNT—ox—DAP—ATC, **Figure 3(D)**, sample demonstrates a 10.7% mass loss and a maximum degradation rate at 297 °C. A comparable pattern is observed. The successful integration of ATC molecules onto the CNT surface is established by the increased mass loss.

When heated to 324 °C and 457 °C, the P(EDOT-co-Py) copolymer, **Figure 3(E)**, breaks down in two main ways, losing 63% and 32% of its mass, respectively. Correspondingly, the thermo-oxidative

 doi:10.20944/preprints202512.1852.v1

degradation of the copolymer is responsible for these events. According to earlier research, P(EDOT-co-Py) has thermal stability in the middle of that of its corresponding homopolymers [74].

The P(EDOT-co-Py)@MWCNT hybrid, **Figure 3(F)**, exhibits three primary thermal events. Below 100 °C, the loss of adsorbed water results in the first process. The degradation of the P(EDOT-co-Py) matrix, which has a maximum rate at 319.8 °C and a mass loss of 41.3%, is comparable to that seen for the pure copolymer. An additional 53.4% mass loss occurs during the breakdown of CNTs in the hybrid, which is linked to the final decomposition step at 612 °C. The hybrid's estimated copolymer-to-CNT mass ratio is roughly 0.75:1 based on these data.

Table S5 provides a summary of the findings from the four-probe method used to measure the electronic conductivity of the pristine P(EDOT-co-Py) copolymer and the P(EDOT-co-Py)@MWCNT hybrid. The conductivity of the synthesized copolymer was 0.71 mS cm^{-1}. This value is higher than the one reported by Kadac et al. (2015) [24], which was 0.710 μS m^{-1}. However, the P(EDOT-co-Py)@MWCNT hybrid had a conductivity of 9.48 mS cm^{-2}, which was much better by more than an order of magnitude. This improvement can be attributed to the establishment of interconnected networks between the conducting polymer and the carbon nanotubes, which enables more efficient charge transport.

The TEM images of the hybrid at two different magnifications are displayed in **Figure 4**. As anticipated, the hybrid showed that the copolymer had evenly coated the CNTs along the whole nanotube. **Figure 4 (B)** additionally displays the CNT width of 21.8 and the polymer coating layer. This uniform coating (5.5 to 11.3 nm thickness) agrees with the other details, especially the TGA analysis, which showed a mass ratio of 0.75:1 for the copolymer and CNT. It also explains why the hybrid had better electronic conductivity than the neat copolymer.

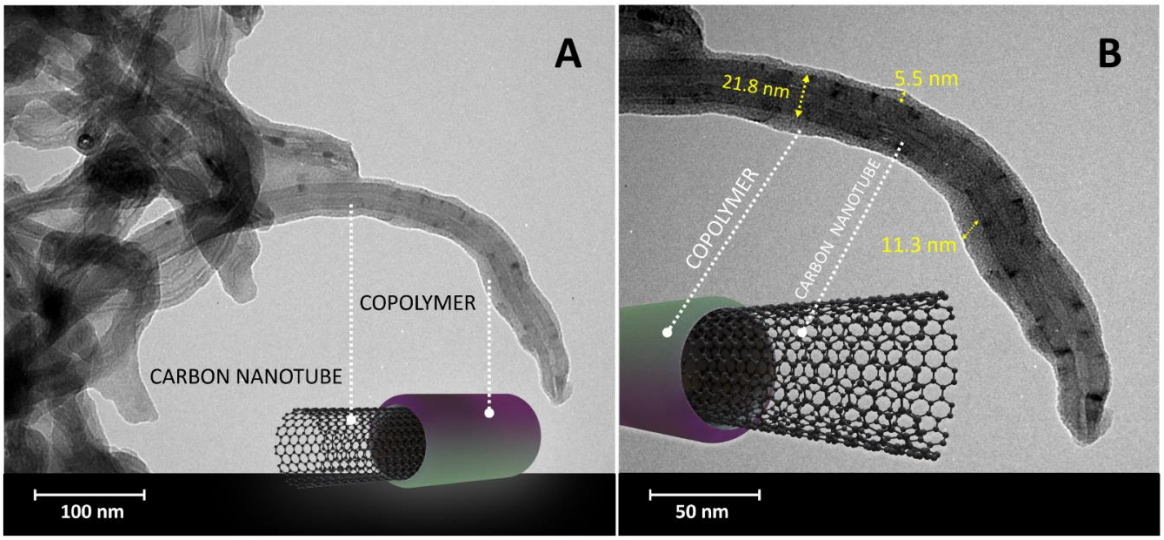

Figure 4. – (A) and (B) TEM image for P(EDOT-co-Py)@MWCNT hybrid.

3.2. Electrochemical Characterization

The electrochemical behavior of the P(EDOT-co-Py)@MWCNT hybrid was investigated in a three-electrode configuration system using aqueous aluminum-based electrolytes. The cyclic voltammetry (CV) curves obtained are shown in **Figure 5**.

 doi:10.20944/preprints202512.1852.v1

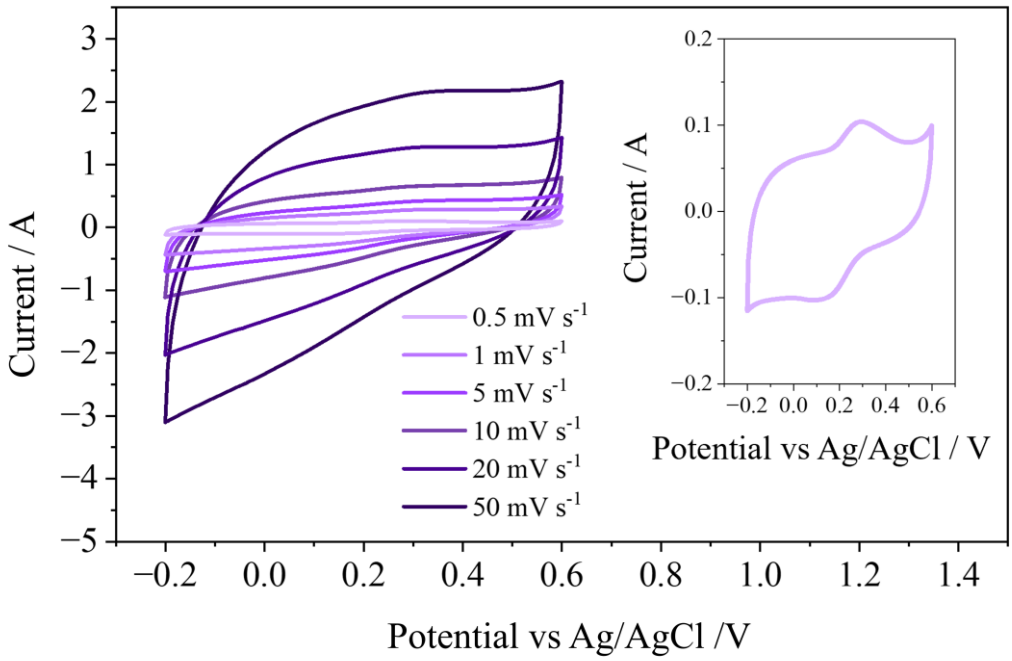

Figure 5. P(EDOT-co-Py)@MWCNT hybrid voltammetry curves at different scan rate (inset 0.5 mV s^{-1}).

At high scan rates, the voltammograms exhibit a characteristic capacitive charge storage behavior. However, at lower ones, the curves display well-defined faradaic features, indicating that the hybrid material operates through two concurrent mechanisms. Under a slow potential scan rate, the predominant process involves redox reactions within the polymer backbone accompanied by the insertion and extraction of Al^{3+} ions, described by equation 5. The cathodic peaks observed (at 0.5 mV s^{-1}) near 0.0 V vs. Ag/AgCl correspond to the reduction of the copolymer and the associated Al^{3+} insertion, while the anodic peaks at 0.33 V vs. Ag/AgCl arise from polymer oxidation and Al^{3+} extraction.

As the scan rate increases, the system becomes dominated by capacitive behavior. This is attributed to proton adsorption on the polymer surface, a faster process than compared to the kinetically limited Al^{3+} insertion, which requires partial desolvation. The protons responsible for this effect originate from the hydrolysis equilibrium of the aluminum aquo-complex, in which $[Al(H_2O)_6]^{3+}$ partially converts into $[Al(H_2O)_5(OH)]^{2+}$ and H_3O^+, equation 6. The coexistence of faradaic and capacitive contributions is consistent with the behavior reported for PEDOT, polypyrrole, and other proton-involving pseudocapacitive polymers. Similar observations have been reported for PEDOT:PSS in aluminum-based electrolytes, where sharp redox peaks and slower Al^{3+} insertion kinetics are predominant at low scan rates, while capacitive proton adsorption takes over at higher rates [14].

$$\mathrm{P(EDOT-co-Py)} + 3e^- + \mathrm{Al^{3+}} \rightleftharpoons \{\mathrm{P(EDOT-co-Py)^{3-}} + \mathrm{Al^{3+}}\} \quad (5)$$

$$[Al(H_2O)_6]^{3+}(aq) + H_2O(aq) \rightleftharpoons [Al(H_2O)_5(OH)]^{2+}(aq) + H_3O^+(aq) \quad (6)$$

The hybrid charge-storage mechanism was further examined by galvanostatic charge–discharge (GCD) measurements, shown in **Figure 6(A)**.

 doi:10.20944/preprints202512.1852.v1

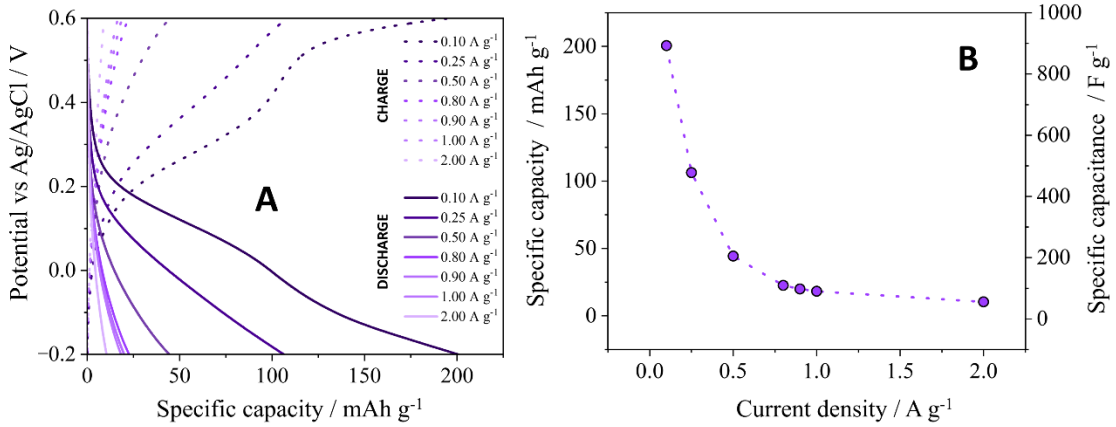

Figure 6. – P(EDOT-co-Py)@MWCNT hybrid (A) GCD curves at different current densities and (B) specific capacity and capacitance values behavior at different current densities.

Unlike voltametric measurements, which are predominantly sensitive to surface-controlled and kinetically fast processes due to the imposed potential sweep, galvanostatic charge–discharge measurements probe the electrode response under a constant current condition, thereby enhancing the contribution of bulk-limited and kinetically slower charge-storage processes. As a result, galvanostatic techniques provide a more representative assessment of the specific capacity or specific capacitance of the electrode material. The GCD curves recorded at different current densities (**Figure 6(A)**) display marked deviations from the ideal linear and symmetric triangular profile expected for purely electrostatic capacitive behavior. In particular, potential regions with reduced slope are observed, indicating the dominance of faradaic processes governed by finite charge-transfer kinetics and ion transport within the polymeric matrix. This kinetic limitation rationalizes the higher capacity values obtained at lower current densities, as shown in **Figure 6(B)**, where extended charge–discharge times allow more complete utilization of the electroactive bulk.

The specific capacities achieved were 200.6, 106.3, 44.3, 19.94, 18.23, and 10.39 mAh g^{-1}, corresponding to 903.0, 478.5, 199.5, 101.7, 89.73, 82.07, and 46.77 F g^{-1} for the current densities of 0.10, 0.25, 0.50, 0.80, 0.90, 1.00, and 2.00 A g^{-1}, respectively. Even at higher current densities, these values surpass those of neat MWCNT electrodes reported of 24.4 F g^{-1} (at 0.25 A g^{-1}) in aqueous electrolyte ($LiClO_4$, 0.5 mol L^{-1}) [31]. Among with the other materials previously reported by our research group, such as the neat copolymers P(EDOT-co-MPy) and P(EDOT-co-PyMP) ($LiClO_4$, 0.5 mol L^{-1}), which reached 69.2 and 64.9 F g^{-1} [38]. A complete electrochemical data for the system is presented **Table S6**.

The data presented in **Table S7** allow a direct comparison with other aqueous aluminum-based energy-storage systems described in the literature. PEDOT:PSS used as the active material in aqueous aluminum-ion batteries operating in 1.2 mol L^{-1} $Al_2(SO_4)_3$ + 0.0025 mol L^{-1} H_2SO_4 delivers specific capacities ranging from 78 to 25 mAh g^{-1} at current densities between 0.20 and 1.00 A g^{-1} [14]. These values are comparable to those obtained for the P(EDOT-co-Py)@MWCNT hybrid, which delivers 106.3 to 18.23 mAh g^{-1} in the 0.25 to 1.00 A g^{-1} range.

Another polymer-based system, polypyrrole@CNT, [37] shows even higher performance, delivering 137 to 112 mAh g^{-1} at 0.25 to 1.00 A g^{-1}. Its superior behavior, particularly at higher current densities, is likely due to the use of a different electrolyte based on an ionic liquid ($AlCl_3$/[EMim]-Cl, 1.3:1 molar ratio). In this configuration, charge storage arises from a combination of the capacitive adsorption/desorption of $AlCl_4^-$ and pseudocapacitive insertion/extraction of the same species. The discrepancy in capacity values compared to the present work is strongly associated with the much wider electrochemical stability window afforded by the ionic-liquid electrolyte (0.3–2.3 V vs Al/Al^{3+}), in contrast to the narrower potential window of –0.2 to 0.6 V vs Ag/AgCl used in this study.

 doi:10.20944/preprints202512.1852.v1

P(EDOT-co-Py)@MWCNT can also be compared with other electrode materials investigated for Al-ion storage applications, such as Prussian Blue analogues. $KCu[Fe(CN)_6]$, synthesized and tested at current densities from 0.05 to 0.40 A g^{-1} in 0.50 mol L^{-1} $Al_2(SO_4)_3$ aqueous electrolyte, delivered specific capacities ranging from 62.9 to 46.9 mAh g^{-1} [8]. These values are lower than those obtained for the hybrid material, which reaches 200.6 mAh g^{-1} at lower current density (0.10 A g^{-1}) and 44.3 mAh g^{-1} at 0.50 A g^{-1}.

Similarly, $K_{0.2}Fe[Fe(CN)_6]_{0.79}{\cdot}2.1H_2O$ tested in 5 m $Al(OTF)_3$ at 0.15 A g^{-1} delivered 116.29 mAh g^{-1} [75], a value that is lower than that of the hybrid at comparable current density, where 200.6 mAh g^{-1} is achieved at 0.10 A g^{-1}. Other Al^{3+} insertion materials have also been investigated in ionic-liquid-based electrolytes, particularly $AlCl_3$/[EMim]-Cl systems. VO_2, for instance, was tested at 0.10 and 0.20 A g^{-1}, delivering 106 to 70 mAh g^{-1} [10], again below the values obtained for the hybrid material developed in this work.

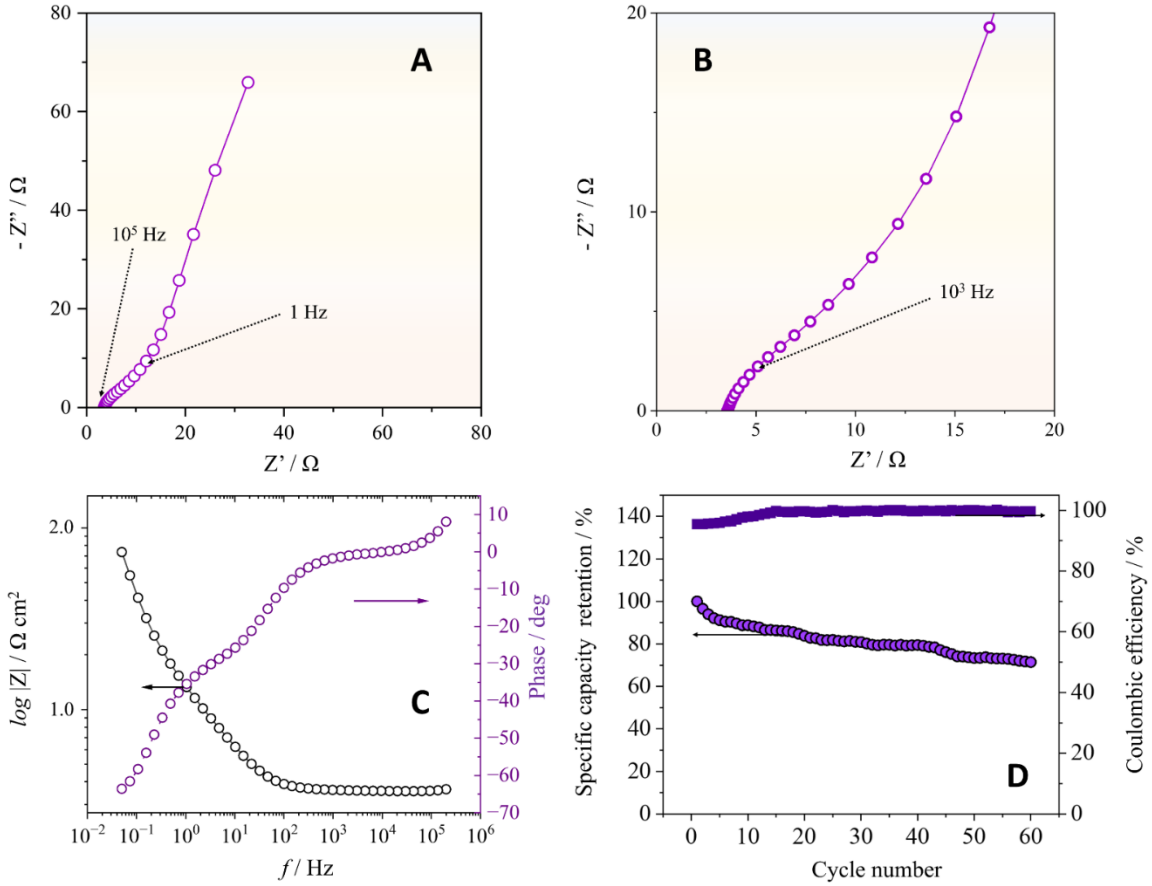

Figure 7. P(EDOT-co-Py)@MWCNT hybrid (A,B) Nyquist and (B) Bode plot. (C) Cycling stability and coulombic efficiency at 0.1 A g^{-1}.

Electrochemical impedance spectroscopy (EIS) was employed to further elucidate the charge-storage mechanism of the P(EDOT-co-Py)@MWCNT hybrid electrode in an aluminum-based aqueous electrolyte. The Nyquist and Bode representations shown in **Figure 7(A, B)** provide complementary and consistent insights into the coexistence of fast surface-controlled pseudocapacitive processes and kinetically constrained faradaic reactions, in agreement with the trends inferred from CV and GCD analyses.

The Nyquist plot (**Figure 7(A)**) exhibits a low intercept on the real axis, corresponding to a small series resistance (R_s = 3.55 Ω). No well-defined semicircle is observed over the medium-frequency range; instead, the impedance rapidly evolves into an inclined tail toward lower frequencies. Such behavior is characteristic of conducting polymer-based electrodes dominated by pseudocapacitive charge storage rather than by classical battery-type responses governed by sluggish charge-transfer

 doi:10.20944/preprints202512.1852.v1

kinetics [76]. A magnified view of the high-frequency region (**Figure 7(B)**) reveals a small and depressed arc, indicating the presence of a charge-transfer process with low but finite resistance. This feature is associated with redox activity along the P(EDOT-co-Py) backbone coupled with the initial stages of Al^{3+} insertion. The depressed nature of the arc reflects the heterogeneous and porous architecture of the polymer–MWCNT hybrid and the resulting distribution of relaxation times. The limited extension of this arc confirms that faradaic reactions contribute to, but do not dominate, the overall impedance response. At lower frequencies, the Nyquist response progressively approaches a quasi-vertical line, deviating from the 45º slope expected for semi-infinite Warburg diffusion. This behavior indicates that long-range diffusion of Al^{3+} ions is not the sole rate-limiting process. Instead, charge storage is largely governed by surface or near-surface processes, consistent with a pseudocapacitive mechanism supplemented by diffusion-assisted faradaic contributions.

This interpretation is further corroborated by the Bode plots, **Figure 7(B)**, which reveal a clear correlation between the impedance magnitude and phase angle across the frequency spectrum. At high frequencies (~10^4 - 10^5 Hz), the impedance magnitude reaches a plateau at low values (|Z| ~ 3 - 4 Ω) while the phase angle remains close to 0° (-2 to -5°), confirming a predominantly ohmic response controlled by electrolyte resistance and electronic conduction through the MWCNT framework. As the frequency decreases into the intermediate–high range (~10^2 – 10^4 Hz), |Z| increases with a slope significantly smaller than −1 in the log|Z| versus log f representation, accompanied by a phase shift toward -20 to -3º. This regime reflects the activation of fast surface-controlled pseudocapacitive processes associated with electronic delocalization and rapid redox transitions within the conjugated polymer chains [76]. In the intermediate–low frequency region (~1 - 100 Hz), the impedance magnitude increases more steeply and the phase angle progressively shifts to -40 to -55º, indicating an increasing contribution from kinetically limited faradaic reactions coupled to partial Al^{3+} insertion into the polymeric matrix. At the lowest frequencies (<1 Hz), |Z| continues to increase without reaching the ideal -1 slope expected for a purely capacitive system, while the phase angle approaches -60 to -65º, evidencing a non-ideal pseudocapacitive response governed by a broad distribution of relaxation times.

Figure 7(C) illustrates the cycling stability of the P(EDOT-co-Py)@MWCNT hybrid over 60 charge–discharge cycles at a current density of 0.1 A g^{-1}. The material retained a specific capacity of 144.43 mAh g^{-1} at the 60th cycle, corresponding to 72% of its initial capacity (200.6 mAh g^{-1}). The coulombic efficiency, which initially reached 96%, increased to 100% by the 15th cycle and remained stable throughout the subsequent cycling, indicating highly reversible electrochemical behavior. The cycling performance of this hybrid material compares favorably with similar Al-ion storage systems reported in the literature.

VS_2 nanosheets [77] were evaluated for 50 cycles using an $AlCl_3$–([EMIm]Cl) ionic liquid electrolyte at 0.1 A g^{-1}. The G-VS_2 electrode retained 88.3 mAh g^{-1} after five cycles and 50 mAh g^{-1} after 100 cycles, corresponding to 47.47% and 26.88% of its initial capacity (186 mAh g^{-1}), respectively. Similarly, a $V_2O_5{\cdot}nH_2O$ cathode tested in an ionic liquid electrolyte delivered 80 mAh g^{-1} after 100 cycles at the same current density, which is significantly lower than the capacity achieved in the present study [78]. In another report, MoS_2 microspheres [79] exhibited a capacity decrease from 77.7 to 66.7 mAh g^{-1} between the 1st and 100th cycles. Although this system showed a higher capacity retention (85.84%), its absolute capacity values were considerably lower than those of the P(EDOT-co-Py)@MWCNT hybrid. Overall, the competitive cycling stability combined with the higher reversible capacity demonstrates that the P(EDOT-co-Py)@MWCNT hybrid is a promising electrode material for Al-ion storage systems, particularly when considering the use of low-cost electrolytes.

4. Conclusions

In this work, a hybrid nanomaterial based on the copolymerization of EDOT and pyrrole chemically anchored onto multiwalled carbon nanotubes was successfully synthesized through a multistep functionalization strategy. The effective surface functionalization of the MWCNTs, the covalent attachment of the monomers, and the formation of a homogeneous P(EDOT-co-Py) coating

 doi:10.20944/preprints202512.1852.v1

along the nanotube surface were confirmed through structural, spectroscopic, thermal, and microscopic characterizations.

Electrochemical evaluation in aqueous aluminum sulfate electrolyte revealed that the P(EDOT-co-Py)@MWCNT hybrid exhibited a high specific capacity, with values reaching 200.6 mAh g^{-1} at 0.10 A g^{-1}, being comparable to or exceeding those reported for several cathode materials for aqueous aluminum-ion storage. The combined Nyquist and Bode analyses demonstrate that charge storage in the P(EDOT-co-Py)@MWCNT electrode arises from the synergistic interplay between fast surface pseudocapacitance and slower insertion-controlled faradaic processes, rather than from a single dominant electrochemical mechanism. Moreover, the hybrid electrode demonstrated good cycling stability, retaining 72% of its initial capacity after 60 cycles and achieving a near 100% coulombic efficiency after initial activation.

Overall, the P(EDOT-co-Py)@MWCNT hybrid emerges as a promising cathode material for aqueous aluminum-ion batteries, combining high reversible capacity, mixed capacitive–faradaic storage behavior, and competitive cycling stability, while relying on low-cost and environmentally benign components. This approach opens new perspectives for the development of advanced polymer-based electrodes for safe and sustainable multivalent energy-storage technologies.

Supplementary Materials: The following supporting information can be downloaded at the website of this paper posted on Preprints.org. **Scheme S1 –** Synthesis of the P(EDOT-co-Py)@MWCNT hybrid steps; **Figure S1 - –** FTIR spectra for MWCNT−ox, MWCNT−ox−DAP and MWCNT−ox−DAP−ATC; **Figure S2 -** FTIR spectra for PEDOT and PPy; **Table S1 -** Raman data for synthesized materials; **Figure S3-** Raman spectra for P(EDOT-co-Py); **Figure S4 -** XPS spectra of S 2p for (A) MWCNT−ox−DAP − ATC and (B) for P(EDOT-co-Py)@MWCNT hybrid; N 1s for (C) MWCNT−ox−DAP − ATC and (D) for P(EDOT-co-Py)@MWCNT hybrid, O 1s for (E) MWCNT−ox−DAP − ATC and (F) for P(EDOT-co-Py)@MWCNT hybrid and C 1s for (G) MWCNT − ox −DAP − ATC and (H) for P(EDOT-co-Py)@MWCNT hybrid; **Table S2 –** Atomic percentage of elements presented in the NTC-ox, NTC-DAP, NTC-DAP–ATC, P(EDOT-co-Py); **Table S3 -** Assignment of photoemission peaks obtained from the deconvolution of XPS spectra in the C 1s and O 1s regions of the samples MWCNT−ox−DAP − ATC and P(EDOT-co-Py)@MWCNT hybrid; **Table S4 -** Atomic percentages of carbon bonds. Assignment of photoemission peaks obtained from the deconvolution of XPS spectra in the C 1s and O 1s regions of the MWCNT−ox−DAP − ATC and P(EDOT-co-Py)@MWCNT hybrid; **Table S5 -** Electrical resistance, resistivity, and conductivity of hybrids and copolymers using the four-point probe method; **Table S6 -** Electrochemical data calculated from the galvanostatic charge/discharge curves for the P(EDOT-co-Py)@MWCNT hybrid electrode using $Al_2(SO_4)_3$ + H_2SO_4 as electrolyte; **Table S7** – Capacity value comparison of the P(EDOT-co-Py)@MWCNT hybrid with other reported Al-ion insertion material.

Author Contributions: Glenda R. B. S. Lacerda: Investigation, formal analysis, Writing – original draft; **Luiz P. F. dos Santos:** Investigation, Formal analysis; **Nathany L.O. Sousa:** Investigation, Formal analysis; **Gabriel J. P. Tonon:** Investigation, formal analysis, Writing – original draft; **Maria L. M. Rocco:** Investigation, Formal analysis; **Túlio Matencio:** Supervision, Resources, Conceptualization, Methodology, **Hállen D. R. Calado:** Supervision, Resources, Conceptualization, Methodology, **Paulo F. R. Ortega:** Visualization, Supervision, Resources, Investigation, Funding acquisition, Conceptualization, Methodology, Project administration, Writing – review & editing, Writing – original draft; **Garbas A. dos Santos Junior:** Visualization, Supervision, Resources, Investigation, Funding acquisition, Conceptualization, Methodology, Project administration, Writing – review & editing, Writing – original draft.

Data Availability Statement: The data presented in this study are available on request from the corresponding author due to authors' rights.

Acknowledgments: This work was supported by Fundação de Amparo à Pesquisa do Estado de Minas Gerais – FAPEMIG (grants APQ-03785-25 and APQ-01313–24). The authors also thank the Laboratory Infrastructure Project of the Chemistry Department at UEMG – Divinópolis Campus (Agreement 144/2021 - 2350.01.0010721/2021 – 92) and acknowledge the Center of Microscopy at the Universidade Federal de Minas Gerais (http://www.microscopia.ufmg.br) for providing the equipment and technical support for experiments

 doi:10.20944/preprints202512.1852.v1

involving electron microscopy. G. R. B; S. Lacerda acknowledges the Conselho Nacional de Desenvolvimento Científico e Tecnológico – CNPq and H. D. R.Calado acknowledges the Instituto Nacional de Ciência e Tecnologia em Nanomateriais de Carbono– INCT Nanocarbono.

Conflicts of Interest: The authors declare no conflicts of interest.

Abbreviations

The following abbreviations are used in this manuscript:

EDOT	3,4-ethylenedioxythiophene
Py	pyrrole
MWCNT	multi-walled carbon nanotubes
TGA	thermogravimetric analysis
FTIR	Fourier-transform infrared spectroscopy
XPS	X-ray photoelectron spectroscopy
TEM	transmission electron microscopy
P(EDOT-co-Py)@MWCNT hybrid	(poly(3,4-ethylenedioxythiophene-co-pyrrol)@MWCNT hybrid
LIBs	lithium-ion batteries
AIBs	aluminum-ion batteries
AISCs	aluminum-ion supercapacitors
PBAs	Prussian Blue Analogues
CP	conducting polymer
PSS	poly(4-styrenesulfonate
PAc	polyacetylene
PANI	polyaniline
PPP	poly(p-phenylene)
PPV	poly(p-phenylenevinylene),
PTh	polythiophene
CNTs	carbon nanotubes
SWCNTs	single-walled carbon nanotubes
$AlCl_3$–[EMIm]Cl	1-Ethyl-3-methylimidazolium chloride-aluminum chloride
(P(EDOT-co-PyMP)	poly(3,4-ethylenedioxythiophene-co-3-(pyrrol-1-methyl)pyridine)
(P(EDOT-co-MPy)	poly(3,4-ethylenedioxythiophene-co-methylpyrrole)
CV	cyclic voltammetry
GCD	galvanostatic charge–discharge
EIS	electrochemical impedance spectroscopy
DAP	1,3-diaminopropane
TCC	3-thiophene carbonyl chloride
PTFE	Polytetrafluoroethylene
NMP	N-methyl-2-pyrrolidone
PVDF	polyvinylidene fluoride
C_{sp}	Specific capacitance
E_{sp}	energy density

 doi:10.20944/preprints202512.1852.v1

P_{sp}	power density
ε	coulombic efficiency
I	
t	
V	
m	
$V_{discharge}$	end of the discharge, after the ohmic drop
dTG	

References

1. M. Kazazi, P. Abdollahi, M. Mirzaei-Moghadam, High surface area TiO_2 nanospheres as a high-rate anode material for aqueous aluminium-ion batteries, *Solid State Ionics*, **2017**, *300*, 32–37.
2. M.R. Palacin, P. Johansson, R. Dominko, B. Dlugatch, D. Aurbach, Z. Li, M. Fichtner, O. Lužanin, J. Bitenc, Z. Wei, C. Glaser, J. Janek, A. Fernández-Barquín, A.R. Mainar, O. Leonet, I. Urdampilleta, J.A. Blázquez, D.S. Tchitchekova, A. Ponrouch, P. Canepa, G.S. Gautam, R.S.R.G. Casilda, C.S. Martinez-Cisneros, N.U. Torres, A. Varez, J.-Y. Sanchez, K.V. Kravchyk, M.V. Kovalenko, A.A. Teck, H. Shiel, I.E.L. Stephens, M.P. Ryan, E. Zemlyanushin, S. Dsoke, R. Grieco, N. Patil, R. Marcilla, X. Gao, C.J. Carmalt, G. He, M.-M. Titirici, Roadmap on multivalent batteries, *J. Phys. Energy*, **2024**, *6*, 031501.
3. N. Melzack, R.G.A. Wills, A Review of Energy Storage Mechanisms in Aqueous Aluminium Technology, *Front. Chem. Eng.*, **2022**, 4, 778265.
4. A.K.X. Tan, S. Paul, Beyond Lithium: Future Battery Technologies for Sustainable Energy Storage, *Energies*, **2024**, *17*, 5768.
5. K. Li, Y. Shao, S. Liu, Q. Zhang, H. Wang, Y. Li, R.B. Kaner, Aluminum-Ion-Intercalation Supercapacitors with Ultrahigh Areal Capacitance and Highly Enhanced Cycling Stability: Power Supply for Flexible Electrochromic Devices, *Small*, **2017**, *13*, 1700380.
6. W. Pan, Y. Zhao, J. Mao, Y. Wang, X. Zhao, K.W. Leong, S. Luo, X. Liu, H. Wang, J. Xuan, S. Yang, Y. Chen, D.Y.C. Leung, High-Energy SWCNT Cathode for Aqueous Al-Ion Battery Boosted by Multi-Ion Intercalation Chemistry, Advanced Energy Materials, **2011**, *11*, 2101514.
7. Z.A. Zafar, S. Imtiaz, R. Razaq, S. Ji, T. Huang, Z. Zhang, Y. Huang, J.A. Anderson, Cathode materials for rechargeable aluminum batteries: current status and progress, J. Mater. Chem. A, **2017**, *5*, 5646–5660.
8. S. Liu, G.L. Pan, G.R. Li, X.P. Gao, Copper hexacyanoferrate nanoparticles as cathode material for aqueous Al-ion batteries, J. Mater. Chem. A, **2015**, *3*, 959–962.
9. J. Jiang, H. Li, T. Fu, B.-J. Hwang, X. Li, J. Zhao, One-Dimensional $Cu_{2-x}Se$ Nanorods as the Cathode Material for High-Performance Aluminum-Ion Battery, ACS Appl. Mater. Interfaces, **2018**, *10*, 17942–17949.
10. W. Wang, B. Jiang, W. Xiong, H. Sun, Z. Lin, L. Hu, J. Tu, J. Hou, H. Zhu, S. Jiao, A new cathode material for super-valent battery based on aluminium ion intercalation and deintercalation, Sci Rep, **2013**, *3*, 3383.
11. J. Joseph, J.F.S. Fernando, M.A. Sayeed, C. Tang, D. Golberg, A. Du, K. (Ken) Ostrikov, A.P. O'Mullane, Exploring Aluminum-Ion Insertion into Magnesium-Doped Manjiroite (MnO_2) Nanorods in Aqueous Solution, ChemElectroChem, **2021**, *8*, 1048–1054.
12. C. Legein, B.J. Morgan, F. Fayon, T. Koketsu, J. Ma, M. Body, V. Sarou-Kanian, X. Wei, M. Heggen, O.J. Borkiewicz, P. Strasser, D. Dambournet, Atomic Insights into Aluminium-Ion Insertion in Defective Anatase for Batteries, Angew Chem Int Ed, **2020**, *59*, 19247–19253.
13. F. Nacimiento, M. Cabello, R. Alcántara, P. Lavela, J.L. Tirado, NASICON-type Na3V2(PO4)3 as a new positive electrode material for rechargeable aluminium battery, Electrochimica Acta, **2018**, *260*, 798–804.
14. Y. Ai, X. Zhang, R. Li, Y. Lan, Y. Zhao, H. Ling, F. Zhang, C. Zhi, X. Bai, W. Wang, Reversible Intercalation of Al-Ions in Poly(3,4-Ethylenedioxythiophene):Poly(4-Styrenesulfonate) Electrode for Aqueous Electrochemical Capacitors with High Energy Density, Energy Tech, **2021**, *9*, 2001036.
15. W. Li, Y. Gu, Y. Zheng, B. Zhu, Y. Liu, Y. Fu, J. Shi, W. Tang, High-rate and long-cycle sodium dual-ion batteries via extended π-conjugated polymer for −45-60 °C operation, Chemical Engineering Journal, **2025**, *520*, 166152.

 doi:10.20944/preprints202512.1852.v1

16. V.J. Vipu Vinayak, K. Deshmukh, V.R.K. Murthy, S.K.K. Pasha, Conducting polymer based nanocomposites for supercapacitor applications: A review of recent advances, challenges and future prospects, Journal of Energy Storage, **2024**, *100*, 113551.
17. U.D. Chavan, P. Prajith, B. Kandasubramanian, Polypyrrole based cathode material for battery application, Chemical Engineering Journal Advances, **2022**, *12*, 100416.
18. S. Meer, A. Kausar, T. Iqbal, Trends in Conducting Polymer and Hybrids of Conducting Polymer/Carbon Nanotube: A Review, Polymer-Plastics Technology and Engineering, **2016**, *55*, 1416–1440.
19. H. Wen, Y. Shi, B. Yin, H. Wen, H. Li, Y. Yao, S. Zhang, T. Ma, Conductive polymer networks: enabling high-performance zinc-ion batteries via dual-ion storage mechanism and structural suppression, Applied Surface Science, **2025**, *713*, 164351.
20. L. Groenendaal, F. Jonas, D. Freitag, H. Pielartzik, J.R. Reynolds, Poly(3,4-ethylenedioxythiophene) and Its Derivatives: Past, Present, and Future, Adv. Mater., **2000**, *12*, 481–494.
21. K.D. Fong, T. Wang, S.K. Smoukov, Multidimensional performance optimization of conducting polymer-based supercapacitor electrodes, Sustainable Energy Fuels, **2017**, *1*, 1857–1874.
22. T. Zhang, J. Wu, F. Ran, Poly(3, 4-Ethylenedioxythiophene) as Promising Energy Storage Materials in Zinc-Ion Batteries, Macromol. Rapid Commun., **2024**, *45*, 2400476.
23. R. Dallaev, Conductive Polymer Thin Films for Energy Storage and Conversion: Supercapacitors, Batteries, and Solar Cells, Polymers, **2025**, *17*, 2346.
24. K. Kadac, A. Nowaczyk, J. Nowaczyk, Synthesis and characterization of new copolymer of pyrrole and 3,4-ethylenedioxythiophene synthesized by electrochemical route, Synthetic Metals, **2015**, *206*, 145–153.
25. J. Brodský, L. Migliaccio, I. Sahalianov, O. Zítka, P. Neužil, I. Gablech, Advancements in PEDOT-based electrochemical sensors for water quality monitoring: From synthesis to applications, TrAC Trends in Analytical Chemistry, **2025**, *183*, 118115.
26. F. Yu, X. Chen, J. Huang, H. Jiang, W. Chen, Y. Chen, Molecular size matching of dopant in polypyrrole and anion in dual-ion battery enhancing the energy storage ability and dynamics of polypyrrole cathode, Chemical Engineering Journal, **2025**, *510*, 161471.
27. Y. Huang, H. Li, Z. Wang, M. Zhu, Z. Pei, Q. Xue, Y. Huang, C. Zhi, Nanostructured Polypyrrole as a flexible electrode material of supercapacitor, Nano Energy, **2016**, *22*, 422–438.
28. G.Z. Chen, Understanding supercapacitors based on nano-hybrid materials with interfacial conjugation, Progress in Natural Science: Materials International, **2013**, *23*, 245–255.
29. A. Sanmugam, C. Vanitha, A.I. Almansour, K. Karuppasamy, T. Maiyalagan, H.-S. Kim, D. Vikraman, A. Alfantazi, Unveiling the PEDOT-polypyrrole hybrid electrode for the electrochemical sensing of dopamine, Sci Rep, **2025**, *15*, 10989.
30. T. Xue, P. Liu, J. Zhang, J. Xu, G. Zhang, P. Zhou, Y. Li, Y. Zhu, X. Lu, Y. Wen, Multiwalled Carbon Nanotube-N-Doped Graphene/Poly(3,4-ethylenedioxythiophene):Poly(styrenesulfonate) Nanohybrid for Electrochemical Application in Intelligent Sensors and Supercapacitors, ACS Omega, **2020**, *5*, 28452–28462.
31. G.R.D.B.S. Lacerda, G.A. Dos Santos Junior, M.L.M. Rocco, R.L. Lavall, T. Matencio, H.D.R. Calado, Development of a new hybrid CNT-TEPA@poly(3,4-ethylenedioxythiophene-co-3-(pyrrol-1-methyl)pyridine) for application as electrode active material in supercapacitors, Polymer, **2020**, *194*, 122368.
32. J. Nong, P.M. Glassman, V.V. Shuvaev, S. Reyes-Esteves, H.C. Descamps, R.Y. Kiseleva, T.E. Papp, M.-G. Alameh, Y.K. Tam, B.L. Mui, S. Omo-Lamai, M.E. Zamora, T. Shuvaeva, E. Arguiri, X. Gong, T.V. Brysgel, A.W. Tan, A.G. Woolfork, A. Weljie, C.A. Thaiss, J.W. Myerson, D. Weissman, S.E. Kasner, H. Parhiz, V.R. Muzykantov, J.S. Brenner, O.A. Marcos-Contreras, Targeting lipid nanoparticles to the blood-brain barrier to ameliorate acute ischemic stroke, Molecular Therapy, **2024**, *32*, 1344–1358.
33. Z. Wang, N. Bramnik, S. Roy, G. Di Benedetto, J.L. Zunino, S. Mitra, Flexible zinc–carbon batteries with multiwalled carbon nanotube/conductive polymer cathode matrix, Journal of Power Sources, **2013**, *237*, 210–214.
34. Q. Meng, K. Cai, Y. Chen, L. Chen, Research progress on conducting polymer based supercapacitor electrode materials, Nano Energy, **2017**, *36*, 268–285.
35. A.S. Pillai, S.M. Varghese, R.B. Rakhi, S.K. Peethambharan, Synergistic effect of solvent addition and temperature treatment on conductivity enhancement of MWCNTs: PEDOT:PSS composite ink for

 doi:10.20944/preprints202512.1852.v1

electrodes in all printed solid-state micro-supercapacitors, Chemical Engineering Journal, **2024**, *495*, 153495.

36. H. Jiao, J. Wang, J. Tu, H. Lei, S. Jiao, Aluminum-Ion Asymmetric Supercapacitor Incorporating Carbon Nanotubes and an Ionic Liquid Electrolyte: Al/$AlCl_3$ -[EMIm]Cl/CNTs, Energy Tech, **2016**, *4*, 1112–1118.
37. D. Kong, M. Zhou, Q. Zhang, X. Wang, J. Yin, M. Zhao, D. Xie, K. Xie, Y. Cui, Q. Li, C. Li, Polypyrrole @ carbon nanotube as a long-life positive electrode for aluminum-ion batteries, Materials Letters, **2025**, *390*, 138398.
38. G.R.D.B.S. Lacerda, G.A. Dos Santos Junior, M.L.M. Rocco, R.L. Lavall, T. Matencio, H.D.R. Calado, Development of nanohybrids based on carbon nanotubes/P(EDOT-co-MPy) and P(EDOT-co-PyMP) copolymers as electrode materials for aqueous supercapacitors, Electrochimica Acta, **2020**, *335*, 135637.
39. W. Gerrard and, M. Thrush, Reactions in Carboxylic Acid-Thionyl Chloride Systems, J. Chem. Soc, **1953**, 2117-2120.
40. H.T. Nguyen, M.T. Chau, P.T.B. Thao, L.T. Nhan, Near-electrode effects of ferroelectric nanocomposites filled with pristine and oxidized multiwalled carbon nanotubes at low frequencies, Ferroelectrics, **2023**, *602*, 174–183.
41. M. Šolić, S. Maletić, M.K. Isakovski, J. Nikić, M. Watson, Z. Kónya, S. Rončević, Removing low levels of Cd(II) and Pb(II) by adsorption on two types of oxidized multiwalled carbon nanotubes, Journal of Environmental Chemical Engineering, **2021**, *9*, 105402.
42. J. Gao, M. Song, T. Li, Y. Zhao, A. Wang, Water-soluble carboxymethyl chitosan (WSCC)-modified single-walled carbon nanotubes (SWCNTs) provide efficient adsorption of Pb(II) from water, RSC Adv., **2022**, *12*, 6821–6830.
43. K. Rahimi, S. Riahi, M. Abbasi, Z. Fakhroueian, Modification of multi-walled carbon nanotubes by 1,3-diaminopropane to increase CO2 adsorption capacity, Journal of Environmental Management, **2019**, *242*, 81–89.
44. T.S. Mirmiran, S. Riahi, M. Abbasi, M. Mohammadi-Khanaposhtani, Synergistic improvement of CO_2 adsorption using functionalized MWCNTs by a simultaneous combination of two amines, Journal of Environmental Chemical Engineering, **2025**, *13*, 119213.
45. Q. Zhao, R. Jamal, L. Zhang, M. Wang, T. Abdiryim, The structure and properties of PEDOT synthesized by template-free solution method, Nanoscale Res Lett, **2014**, *9*, 557.
46. H. Liu, W. Zhou, X. Ma, S. Chen, S. Ming, K. Lin, B. Lu, J. Xu, Capacitive performance of electrodeposited PEDOS and a comparative study with PEDOT, Electrochimica Acta, **2016**, *220*, 340–346.
47. D. Hewidy, A.-S. Gadallah, G.A. Fattah, Electroluminescence enhancement of glass/ITO/PEDOT:PSS/MEH-PPV/PEDOT:PSS/Al OLED by thermal annealing, Journal of Molecular Structure, **2017**, *1130*, 327–332..
48. H. Li, X. Sun, D. Liu, X. Liu, X. Du, S. Li, X. Xing, X. Cheng, D. Bi, D. Qiu, Facile Synthesis of Novel Conducting Copolymers Based on N-Furfuryl Pyrrole and 3,4-Ethylenedioxythiophene with Enhanced Optoelectrochemical Performances Towards Electrochromic Application, Molecules, **2024**, *30*, 42.
49. M.M. Rahman, I. Alam, M.R. Hossen, F. Azim, N. Anjum, M.O. Faruk, M.M. Rahman, O.I. Okoli, Facile Synthesis of Conductive Copolymers and Its Supercapacitor Application, J. Compos. Sci., **2025**, *9*, 253.
50. M.E. Martínez-Cartagena, J. Bernal-Martínez, A. Banda-Villanueva, I. Magaña, T. Córdova, A. Ledezma-Pérez, S. Fernández-Tavizón, R. Díaz De León, A Comparative Study of Biomimetic Synthesis of EDOT-Pyrrole and EDOT-Aniline Copolymers by Peroxidase-like Catalysts: Towards Tunable Semiconductive Organic Materials, Front. Chem., **2022**, *10*, 915264.
51. A.-B. Al-Odayni, F.S. Alsubaie, N.A.Y. Abdu, H.M. Al-Kahtani, W.S. Saeed, Adsorption Kinetics of Methyl Orange from Model Polluted Water onto N-Doped Activated Carbons Prepared from N-Containing Polymers, Polymers, **2023**, *15*, 1983.
52. M.M. Rahman Khan, M. Islam, Md.K. Amin, S.K. Paul, S. Rahman, Md.M. Talukder, Md.M. Rahman, Simplistic fabrication of aniline and pyrrole-based poly(Ani-co-Py) for efficient photocatalytic performance and supercapacitors, International Journal of Hydrogen Energy, **2022**, *47*, 37860–37869.

 doi:10.20944/preprints202512.1852.v1

53. F. López-García, G. Canché-Escamilla, A.L. Ocampo-Flores, P. Roquero-Tejeda, L.C. Ordóñez, Controlled Size Nano-Polypyrrole Synthetized in Micro-Emulsions as Pt Support for the Ethanol Electro-Oxidation Reaction, International Journal of Electrochemical Science, **2013**, *8*, 3794–3813.
54. K.S. Pasupuleti, N.-H. Bak, K.R. Peta, S.-G. Kim, H.D. Cho, M.-D. Kim, Enhanced sensitivity of langasite-based surface acoustic wave CO gas sensor using highly porous Ppy@PEDOT:PSS hybrid nanocomposite, Sensors and Actuators B: Chemical 363 (2022) 131786.
55. A.S. Sarac, G.S. Nmez, F.C. Cebeci, Electrochemical synthesis and structural studies of polypyrroles, poly(3,4-ethylene-dioxythiophene)s and copolymers of pyrrole and 3,4-ethylenedioxythiophene on carbon fibre microelectrodes, j. of Applied Electrochemistry, **2003**, *33*, 295-301.
56. H. Zhu, M. Li, D. Wang, S. Zhou, C. Peng, Interfacial Synthesis of Free-Standing Asymmetrical PPY-PEDOT Copolymer Film with 3D Network Structure for Supercapacitors, J. Electrochem. Soc., **2017**, *164*, A1820–A1825.
57. C.F. Hsu, L. Zhang, H. Peng, J. Travas-Sejdic, P.A. Kilmartin, Free radical scavenging properties of polypyrrole and poly(3,4-ethylenedioxythiophene), Current Applied Physics, **2008**, *8*, 316–319.
58. S. Kulandaivalu, Z. Zainal, Y. Sulaiman, Influence of Monomer Concentration on the Morphologies and Electrochemical Properties of PEDOT, PANI, and PPy Prepared from Aqueous Solution, International Journal of Polymer Science, **2016**, *2016*, 1–12.
59. M.E. Martínez-Cartagena, J. Bernal-Martínez, A. Banda-Villanueva, I. Magaña, T. Córdova, A. Ledezma-Pérez, S. Fernández-Tavizón, R. Díaz De León, A Comparative Study of Biomimetic Synthesis of EDOT-Pyrrole and EDOT-Aniline Copolymers by Peroxidase-like Catalysts: Towards Tunable Semiconductive Organic Materials, Front. Chem., **2022**, *10*, 915264.
60. S. Radhakrishnan, C. Sumathi, A. Umar, S. Jae Kim, J. Wilson, V. Dharuman, Polypyrrole–poly(3,4-ethylenedioxythiophene)–Ag (PPy–PEDOT–Ag) nanocomposite films for label-free electrochemical DNA sensing, Biosensors and Bioelectronics, **2013**, *47*, 133–140.
61. M. Lay, M.À. Pèlach, N. Pellicer, J.A. Tarrés, K.N. Bun, F. Vilaseca, Smart nanopaper based on cellulose nanofibers with hybrid PEDOT:PSS/polypyrrole for energy storage devices, Carbohydrate Polymers, **2017**, *165*, 86–95.
62. S.B. Brachetti-Sibaja, D. Palma-Ramírez, A.M. Torres-Huerta, M.A. Domínguez-Crespo, H.J. Dorantes-Rosales, A.E. Rodríguez-Salazar, E. Ramírez-Meneses, CVD Conditions for MWCNTs Production and Their Effects on the Optical and Electrical Properties of PPy/MWCNTs, PANI/MWCNTs Nanocomposites by In Situ Electropolymerization, Polymers, **2021**, *13*, 351.
63. L. Vellingiri, K. Annamalai, R. Kandasamy, I. Kombiah, Characterization and hydrogen storage properties of SnO2 functionalized MWCNT nanocomposites, International Journal of Hydrogen Energy, **2018**, *43*, 10396–10409.
64. T.L.D.A. Montanheiro, F.H. Cristóvan, J.P.B. Machado, D.B. Tada, N. Durán, A.P. Lemes, Effect of MWCNT functionalization on thermal and electrical properties of PHBV/MWCNT nanocomposites, J. Mater. Res., **2015**, *30*, 55–65.
65. E.R. Edwards, S.S. Oishi, E.C. Botelho, Analysis of chemical polymerization between functionalized MWCNT and poly(furfuryl alcohol) composite, Polímeros, **2018**, *28*, 15–22.
66. S.-L. Zhang, C. Qing, R. Zhang, S.-Q. Wu, Z.-H. Xu, Y.-H. Wang, K. Du, Q.-J. Yin, rGO/CNTs/PEDOT: PSS ternary composites with enhanced thermoelectric properties, Synthetic Metals, **2023**, *300*, 117493.
67. P. Chakraborty, S. Mandal, A. Sarkar, K. Kargupta, D. Banerjee, Pure organic dual phase polypyrrole wrapped single-walled carbon nanotube hybrid nano-photocatalyst for solar hydrogen generation, Journal of Photochemistry and Photobiology A: Chemistry, **2025**, *462*, 116210.
68. A.P.P. Alves, J.P.C. Trigueiro, H.D.R. Calado, G.G. Silva, Poly(3-hexylthiophene)-multi-walled carbon nanotube (1:1) hybrids: Structure and electrochemical properties, Electrochimica Acta, **2016**, *209*, 111–120.
69. S.W. Kim, T. Kim, Y.S. Kim, H.S. Choi, H.J. Lim, S.J. Yang, C.R. Park, Surface modifications for the effective dispersion of carbon nanotubes in solvents and polymers, Carbon, **2012**, *50*, 3–33.
70. K. Yang, M. Gu, Y. Guo, X. Pan, G. Mu, Effects of carbon nanotube functionalization on the mechanical and thermal properties of epoxy composites, Carbon, **2009**, *47*, 1723–1737.

 doi:10.20944/preprints202512.1852.v1

71. N. Dasdevan, M.A.A. Mohd Abdah, Y. Sulaiman, Facile Electrodeposition of Poly(3,4-ethylenedioxythiophene) on Poly(vinyl alcohol) Nanofibers as the Positive Electrode for High-Performance Asymmetric Supercapacitor, Energies, **2019**, *12*, 3382.
72. W.M. Silva, H. Ribeiro, L.M. Seara, H.D.R. Calado, A.S. Ferlauto, R.M. Paniago, C.F. Leite, G.G. Silva, Surface properties of oxidized and aminated multi-walled carbon nanotubes, J. Braz. Chem. Soc., **2012**, *23*, 1078–1086.
73. J.P.C. Trigueiro, G.G. Silva, R.L. Lavall, C.A. Furtado, S. Oliveira, A.S. Ferlauto, R.G. Lacerda, L.O. Ladeira, J.-W. Liu, R.L. Frost, G.A. George, Purity Evaluation of Carbon Nanotube Materials by Thermogravimetric, TEM, and SEM Methods, J. Nanosci. Nanotech., **2007**, *7*, 3477–3486.
74. Y. Jin, Q. Chen, P. Lessner, Thermal Stability Investigation of PEDOT Films from Chemical Oxidation and Prepolymerized Dispersion, Electrochemistry, **2013**, *81*, 801–803.
75. A. Zhou, L. Jiang, J. Yue, Y. Tong, Q. Zhang, Z. Lin, B. Liu, C. Wu, L. Suo, Y.-S. Hu, H. Li, L. Chen, Water-in-Salt Electrolyte Promotes High-Capacity $FeFe(CN)_6$ Cathode for Aqueous Al-Ion Battery, ACS Appl. Mater. Interfaces, **2019**, *11*, 41356–41362.
76. M. Ates, Review study of electrochemical impedance spectroscopy and equivalent electrical circuits of conducting polymers on carbon surfaces, Progress in Organic Coatings, **2011**, *71*, 1–10.
77. L. Wu, R. Sun, F. Xiong, C. Pei, K. Han, C. Peng, Y. Fan, W. Yang, Q. An, L. Mai, A rechargeable aluminum-ion battery based on a VS_2 nanosheet cathode, Phys. Chem. Chem. Phys., **2018**, *20*, 22563–22568.
78. H. Wang, X. Bi, Y. Bai, C. Wu, S. Gu, S. Chen, F. Wu, K. Amine, J. Lu, Open-Structured $V_2O_5 \cdot n\,H_2O$ Nanoflakes as Highly Reversible Cathode Material for Monovalent and Multivalent Intercalation Batteries, Advanced Energy Materials, **2017**, *7*, 1602720.
79. Z. Li, B. Niu, J. Liu, J. Li, F. Kang, Rechargeable Aluminum-Ion Battery Based on MoS_2 Microsphere Cathode, ACS Appl. Mater. Interfaces, **2018**, *10*, 9451–9459.